J. Fluid Mech. (2014), *vol.* 755, *pp.* 62–82. © Cambridge University Press 2014
doi:10.1017/jfm.2014.425

Receptivity of a swept-wing boundary layer to micron-sized discrete roughness elements

Holger B. E. Kurz[1] **and Markus J. Kloker**[1,†]

[1]Institute of Aerodynamics and Gas Dynamics, University of Stuttgart, Pfaffenwaldring 21, D-70550 Stuttgart, Germany

(Received 19 February 2014; revised 16 May 2014; accepted 21 July 2014; first published online 14 August 2014)

The receptivity of a laminar swept-wing boundary layer to a spanwise array of circular roughness elements is investigated by means of direct numerical simulations (DNS). The initial amplitude of a steady crossflow mode generated by the shallow roughness elements does not vary strictly linearly with the roughness height, as often assumed. Rather, a fundamental, superlinear dependence of the receptivity amplitude on the roughness height is found. In order to account for shape effects, the roughness geometry is Fourier decomposed to its spanwise spectral content, and elements with a reduced spectrum are investigated. If only modes are present that synthesise a regular structure of alternating bumps and dimples of equal shape and size, the receptivity amplitude is strictly linear for each mode and nominal roughness heights up to at least 15 % of the local displacement thickness.

Key words: boundary layer receptivity, drag reduction, flow control

1. Introduction

The effect of wall roughness on the evolution of wall-bounded flows is of particular interest for the topical laminar flow control. Generally, low roughness levels are sought to keep the excitation of unstable disturbances small. On the other hand, one application of artificial, ordered roughness is the stabilisation of a swept-wing boundary layers by means of the method of distributed roughness elements, as suggested by Saric, Carrillo & Reibert (1998), see also Wassermann & Kloker (2002), where a control mode is induced by a spanwise array of discrete roughness elements close to the leading edge at an infinite-span wing model. While the downstream development of boundary-layer disturbances nowadays can be well described by stability theories, there is still no universal theory to predict the initial amplitudes generated by discrete surface roughness. Therefore, careful costly experiments or direct numerical simulations (DNS) often constitute the only means to determine these data for a given problem. The motivation for this study was to check recent results that showed a virtually linear increase of excited steady crossflow-mode amplitudes with increasing height of discrete roughness elements, see the experimental

† Email address for correspondence: kloker@iag.uni-stuttgart.de

https://doi.org/10.1017/jfm.2014.425 Published online by Cambridge University Press

studies by Hunt & Saric (2011) and Borodulin *et al.* (2013), and the numerical study by Tempelmann *et al.* (2012). These studies contradict the experiments by Kurian, Fransson & Alfredsson (2011), who found a pronounced quadratic increase.

Roughness-induced boundary-layer perturbations, including the effects of nonlinear roughness heights, have been addressed using large-Reynolds-number asymptotic theories by, among others, Smith *et al.* (1981), Bogolepov (1986), Smith (1991) and Lipatov & Vinogradov (2000). Receptivity of two-dimensional (2D) boundary layers to free-stream disturbances in conjunction with surface roughness was studied by Bodonyi *et al.* (1989), allowing roughness heights that may lead to local flow reversal. For moderate heights, their results indicate superlinear receptivity. The particular case of the excitation of steady crossflow vortices by surface roughness in a 3D boundary layer was investigated by Choudhari & Duck (1996). For increasing roughness height, a larger increase in receptivity than is predicted by linear theory has been found. It is further stated that the nonlinear receptivity becomes apparent well before the stability characteristics of the underlying boundary layer flow are altered. However, the authors do emphasise the need for a verification of their partially tentative findings for moderate Reynolds numbers.

Gaponenko *et al.* (2002) determined experimentally the receptivity characteristics for a swept-wing boundary layer to time-harmonic surface vibrations; frequencies and spanwise wavenumbers were varied. Results for zero-frequency disturbances were obtained by an extrapolation from the unsteady data and found to be in good agreement with theoretical results based on linear receptivity theory; however, a height variation was not explicitly reported. Receptivity for the interaction of free-stream vortical disturbances with steady surface roughness was addressed by Borodulin *et al.* (2013) on a similar set-up. The resulting disturbance mode amplitudes were concluded to be linear functions of the vortex amplitudes or roughness heights, where the height was between 19 and 32 % of the chordwise displacement thickness.

Experiments by Hunt & Saric (2011) also suggest a linear relationship between the height of a surface roughness array and disturbance amplitudes downstream of these elements, as long as the measurements are conducted in the region of presumed ‘linear’ receptivity. For higher elements, nonlinear saturation effects of the disturbance modes on their way to the measuring station lead to decreased amplitude ratios, while the behaviour of the initial amplitudes exactly at the roughness elements remains unclear. In fact, for the smallest roughness heights investigated, a superlinear behaviour appeared, but was not addressed. Tempelmann *et al.* (2012) found linear receptivity to an indirectly meshed spanwise-periodic row of roughness cylinders by means of DNS, as long as the height did not exceed 10 % of the local displacement thickness.

The representation of surface roughness in numerical computations can be accomplished by incorporating the wall geometry into the numerical mesh. However, this often complicates the mesh generation and the numerical treatment. Therefore, it has become customary to model small roughness elements by inhomogeneous boundary conditions along a smooth wall (see, e.g. Hill 1995; Bertolotti 2000), thereby approximately enforcing the no-slip condition at the roughness height. The necessary velocity distribution at the wall is typically obtained from a Taylor series expansion of the disturbance flow field, truncated after the linear term, and projected to the smooth wall. The accuracy of this method can be enhanced by multiplying the nominal roughness height by a correction factor before defining the inhomogeneous boundary conditions. For discrete roughness elements, Luchini (2013) derived a so-called protrusion coefficient to account for aspect ratio effects, i.e. the ratio of

https://doi.org/10.1017/jfm.2014.425 Published online by Cambridge University Press

height to diameter. For increasing roughness height at constant diameter, he found an increasing protrusion coefficient, i.e. a nonlinear connection between roughness height and the prescribed tangential velocity at the wall. When assuming linear receptivity to inhomogeneous boundary disturbances, this leads to a weak 'superlinear' receptivity to surface roughness in this case.

In this work, we perform DNS with meshed roughness elements. In order to scrutinise the receptivity behaviour, we alter the spanwise spectral content of the element geometry. We also compare the receptivity coefficients to the results found when modelling the surface non-uniformities by means of inhomogeneous boundary conditions.

2. Basics of the numerical method

DNS are performed using a sixth-order accurate, compact finite-difference flow solver, solving the time-dependent, three-dimensional, compressible Navier–Stokes equations in a non-dimensional conservative formulation. The basics of the DNS code, including the implemented boundary conditions, can be found in Babucke (2009). For more details on code verification for 3D boundary layers, see Friederich & Kloker (2011) and Friederich & Kloker (2012). (In contrast to those investigations, we use finite-difference discretisation in the periodic spanwise direction and no disturbance formulation.) For information on discretisation and parallelisation, see Keller & Kloker (2013). Derivative computations are performed on a uniformly spaced Cartesian computational grid, therefore requiring a grid transformation technique to account for the actual physical geometry. We compute the required metric coefficients with the same numerical scheme as is used for the derivation of the flow-field variables during the actual simulation, thereby minimising the numerical error. At each time step, derivatives obtained on the computational grid are transformed to physical space and plugged into the untransformed Navier–Stokes equations. For a constant spanwise step size Δz, this procedure enables us to cancel out redundant metric coefficients, making the transformation to physical space less costly. The grid with roughness included is obtained by deforming the grid on the wing through 'lifting' the roughness element from the wall. As a consequence, the mantle of the element has to have a finite slope, i.e. the element is slightly smoothed (see figures 6 and 7). The construction of the numerical grid for the various roughness element cases is described in § 3.3.

A steady solution of the flow past an infinite-span wing profile under consideration is computed with the Reynolds-averaged Navier–Stokes (RANS) solver TAU employing a second-order finite-volume scheme. For a description of the code and recent applications see Schwamborn, Gerhold & Heinrich (2006). The boundary layer is resolved with a structured grid block encircling the wing profile, having approximately 30 grid points across the boundary layer thickness in the region of interest for the subsequent DNS. Free-stream conditions are prescribed on a circular far-field boundary with a radius of 100 chord lengths. Adiabatic boundary conditions are prescribed on the wing surface. Laminar flow upstream of the desired transition location is ensured by locally suppressing the production of eddy viscosity in the RANS solver, therefore technically switching off the turbulence modelling in the laminar region.

The converged TAU solution is interpolated to a 2D high-resolution DNS grid by means of a sixth-order Lagrangian interpolation scheme, herein denoted Ω_0, see figure 1. Care was taken to make sure the surface geometries of both grids coincide,

https://doi.org/10.1017/jfm.2014.425 Published online by Cambridge University Press

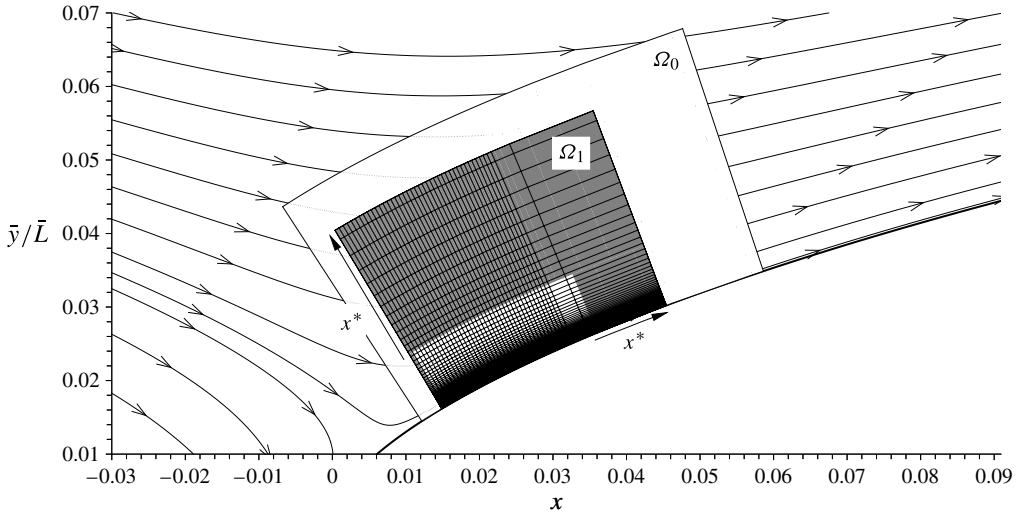


FIGURE 1. Domain Ω_0 used to obtain a first steady DNS solution, and DNS domain Ω_1 for the simulations with roughness elements. 2D streamlines (spanwise velocity component w set to zero) of the TAU base flow in the background. The shown grid lines represent every second wall-parallel and every thirtieth wall-normal line of the fine grid. The grey shading depicts regions with a sponge gain $\mathrm{d}\sigma(x^*) > 0$, cf. (2.1), extending over 25 grid points from inflow, free-stream and outflow boundary, respectively.

avoiding extrapolation issues. The streamwise and wall-normal extent of this domain is somewhat larger than needed for the actual simulations with roughness elements. The result of the interpolation is converged by a steady DNS to account for differences in the numerical schemes and deviations due to the interpolation. Here, we use linearised one-dimensional, unsteady characteristic boundary conditions (Giles 1990) on the inflow and the free-stream boundaries, keeping the time-mean values from the TAU simulation. On these boundaries, outgoing characteristics are extrapolated from the domain interior, while incoming characteristics are set to zero. At the outflow we set second derivatives to zero to permit adjustments of the flow, but fix the pressure for stability. The wall-boundary condition is again set to adiabatic.

In a subsequent step, the streamwise and wall-normal DNS domain extent is reduced to the size used for the actual DNS with roughness elements (domain labelled Ω_1, see figure 1). All boundary conditions are set as before; however, since the new boundaries are located inside the previously used domain, boundary specification data is now obtained from the 2D DNS instead of the TAU solution. Relative deviations in the velocity components between the original TAU data and the converged solution on this set-up are of the order of 10^{-3}, where the maxima occur close to the wall. This final solution serves as the reference state and the initial solution as the conservative variables $\boldsymbol{Q}_b = (\rho_b, \rho_b u_b, \rho_b v_b, \rho_b w_b, E_b)^{\mathrm{T}}$ for all subsequent simulations.

For the 3D unsteady DNS with roughness elements, inflow, free-stream and outflow are treated with the characteristic boundary conditions. In order to minimise reflections, sponge layers forcing the unsteady solution to the reference state are employed in front of these boundaries (cf. Babucke 2009):

$$\frac{\partial \boldsymbol{Q}}{\partial t} = \left.\frac{\partial \boldsymbol{Q}}{\partial t}\right|_{Navier\text{–}Stokes} - \mathrm{d}\sigma(x^*)\left(\boldsymbol{Q} - \boldsymbol{Q}_b\right). \tag{2.1}$$

https://doi.org/10.1017/jfm.2014.425 Published online by Cambridge University Press

Here, the subscript Navier–Stokes denotes the time derivative obtained from evaluation of the full Navier–Stokes equations, the left-hand side is used to advance the scheme in time. The second term on the right-hand side in (2.1) constitutes a source term with a gain factor $d = 3000$ and the spatial distribution function

$$\sigma(x^*) = 6x^{*5} - 15x^{*4} + 10x^{*3}, \quad x^* \in [0, 1], \tag{2.2}$$

where the local coordinate x^* is defined perpendicular to the local domain boundary. Here, x^* is defined such that the sponge regions span 25 grid points from each considered domain boundary. For additional damping of downstream-travelling disturbances, the grid comprises a stretched outflow zone in conjunction with a spatial compact tenth-order low-pass filter (cf. Gaitonde & Visbal 1998), where the chordwise stepsize is increased following a geometric stretching function. Thus, disturbances become successively underresolved due to the increasing stepsize and are strongly attenuated by the spatial filtering (Colonius, Lele & Moin 1993). In combination with the chosen gain factor d, the sponge zones have proved to efficiently minimise reflections for a wide range of boundary-layer disturbances, including fully turbulent flow. The stretched region and sponge layers are excluded from the evaluation of the DNS results. Isothermal boundary conditions are used at the wall, keeping the adiabatic smooth-wall base solution.

3. Flow configuration

3.1. *Base flow*

The base flow under consideration is the compressible flow past a modified infinite-span NACA 671-215 profile with a chord length of $\bar{L} = 2.0$ m (overbar denotes dimensional values), hereafter used as the reference length for the chordwise and tangential coordinates, x and ξ, respectively. All other length scales are non-dimensionalised by $\bar{\delta}_{1,s,R} = 1.7 \times 10^{-4}$ m, the displacement thickness at the roughness position $x = 0.02$, calculated using the definition for compressible flow in the local streamline system. The set-up is used in the EU project 'RECEPT' and is illustrated in figure 2 (inset). The wing profile has an angle of attack of $\alpha = -6.1°$, measured perpendicular to the leading edge, and a sweep angle $\beta = 35°$. A steady base flow was first computed applying TAU with the free-stream velocity $\bar{Q}_\infty = 191.8$ m s^{-1}, serving as reference velocity for non-dimensionalisation. The flow is further characterised by $Ma_\infty = \bar{Q}_\infty/\bar{a}_\infty = 0.65$, where $\bar{a}_\infty$ is the free-stream speed of sound and $Re = \bar{Q}_\infty \bar{\rho}_\infty (\bar{L}/\cos\beta)/\bar{\mu}_\infty = 10.3 \times 10^6$, with the free-stream values of the density $\bar{\rho}_\infty$ and the dynamic viscosity $\bar{\mu}_\infty$. The resulting flow on the considered upper profile side features a stagnation line at $x = 0.01$ and subsequent acceleration up to $x = 0.70$. The distribution of the pressure coefficient $c_p = (p - p_\infty)/(0.5\rho_\infty Q_\infty^2)$ on the upper wing side is given in figure 2. In conjunction with the sweep angle and the resulting crossflow, the accelerated boundary layer on the upper wing side is subject to significant crossflow instability in the absence of Tollmien–Schlichting instability.

The global coordinate x is aligned with the chord, the latter being defined as the shortest distance between leading edge and trailing edge, z coincides with the spanwise direction, and y points upwards to complete the right-handed Cartesian coordinate system. For the investigation of the boundary layer, the introduction of a tangential curvilinear coordinate system is convenient, where ξ is the distance from the leading edge along the surface, η is the wall-normal coordinate and z is again

https://doi.org/10.1017/jfm.2014.425 Published online by Cambridge University Press

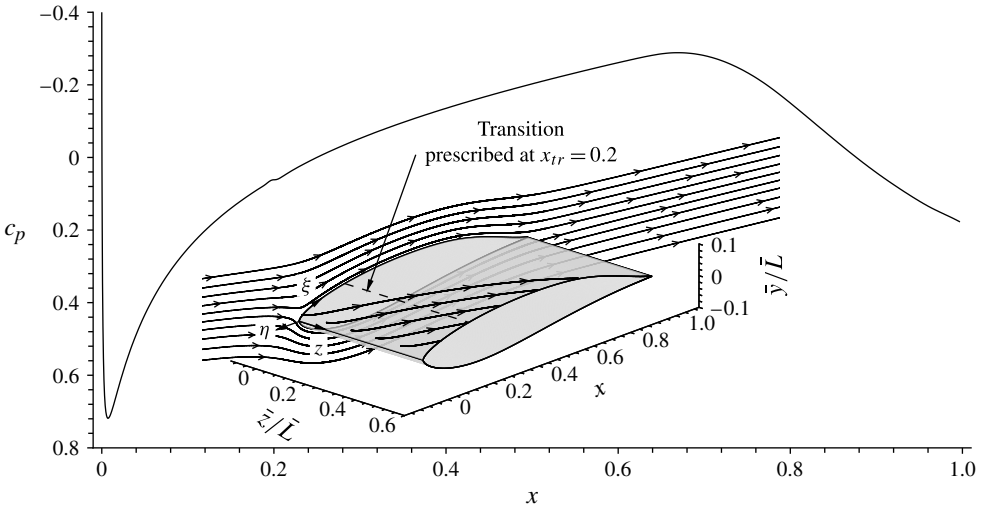


FIGURE 2. Distribution of the pressure coefficient c_p on the upper side of the swept-wing profile. The inset shows 2D streamlines (thin lines, spanwise velocity component w set to zero) and 3D streamlines (thick lines), the latter starting close to the boundary layer edge in the stagnation line region. The dashed line depicts the prescribed transition location $x_{tr} = 0.2$ for the base flow computation. The curvilinear tangential system (ξ, η, z) has its origin at the leading edge.

the spanwise direction, cf. figure 2 (inset). Note that the velocity components u, v and w are associated with the tangential coordinates (ξ, η, z).

The DNS domain Ω_1 is depicted in figure 1 and extends from $x = 0.0150$ to $x = 0.0325$ with uniform grid spacing along the wall, extended by an additional stretched outflow zone up to $x = 0.0454$. The domain height is $0.0283\bar{L}$, corresponding to $333\bar{\delta}_{1,s,R}$. The clustering of grid points close to the wall is relaxed in the wall-normal direction by a geometric stretching function with a variable stretching factor. The spanwise direction z is treated with periodic boundary conditions and covers a range of $\lambda_{z,0} = 23.53$, according to the spanwise wavelength of the most amplified steady crossflow mode, unless otherwise stated. In order to check for effects of the spanwise spacing, a set-up with the wavelength of the control mode (Saric *et al.* 1998) $\lambda_{z,C} = 2/3\lambda_{z,0} = 15.69$ has also been employed. The structured fine grid has $N_\xi = 1258$, $N_\eta = 188$ and $N_z = 128$ points for $\lambda_{z,0}$ and $N_z = 86$ for $\lambda_{z,C}$. For a convergence study with meshed roughness elements and for simulations with modelled roughness, a standard grid has been employed by reducing the resolution by a factor of two in each direction.

Boundary layer parameters for the uniformly spaced extent of the DNS domain are shown in figure 3. The subscript s indicates quantities transformed to a streamline-oriented coordinate system, i.e. rotated about the edge-streamline angle ϕ_e; subscript e denotes quantities at the boundary layer edge. The integral formulation for the compressible displacement thickness

$$\delta_{1,s} = \int_0^{\eta_e} \left(1 - \frac{\rho}{\rho_e}\frac{u_s}{u_{s,e}}\right) \mathrm{d}\eta \tag{3.1}$$

is evaluated up to an approximate boundary layer edge η_e, defined at the wall distance where the total vorticity magnitude falls below 0.5 % of the wall-normal maximum

https://doi.org/10.1017/jfm.2014.425 Published online by Cambridge University Press

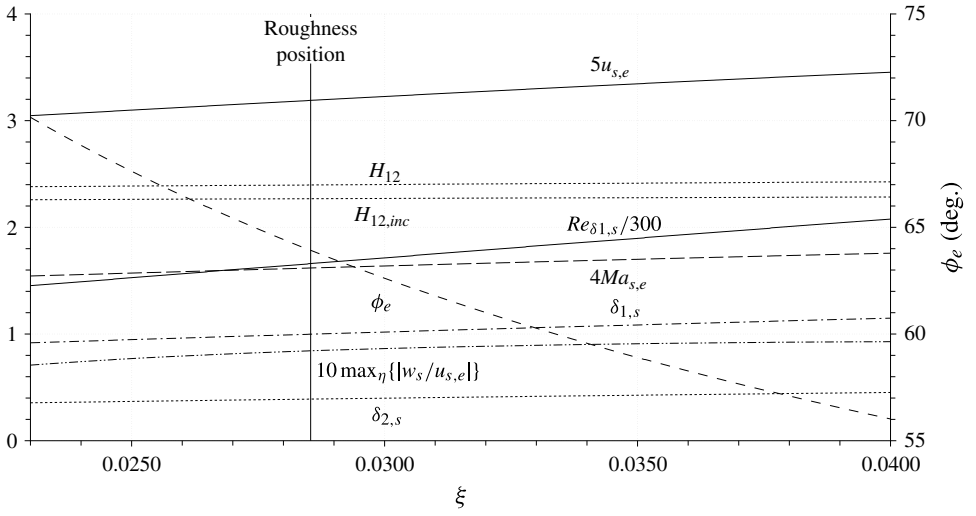


FIGURE 3. Streamline-oriented boundary-layer parameters in the DNS domain: edge velocity $u_{s,e}$, displacement thickness $\delta_{1,s}$, momentum thickness $\delta_{2,s}$, local Reynolds number $Re_{\delta 1,s}$, local edge Mach number $Ma_{s,e}$, maximum of crossflow $\max_\eta\{|w_s/u_{s,e}|\}$, edge-streamline angle ϕ_e. The calculated shape parameter H_{12} ($H_{12,inc}$ calculated with the incompressible definition) in the chordwise system.

across the boundary layer. The necessity for such a bound of integration arises from the flow over a real wing profile, where the values of ρ and u_s are not constant along η outside the boundary layer, therefore prohibiting an integration to infinity. Accordingly, the compressible momentum thickness is calculated as

$$\delta_{2,s} = \int_0^{\eta_e} \frac{\rho}{\rho_e}\frac{u_s}{u_{s,e}}\left(1-\frac{u_s}{u_{s,e}}\right)\mathrm{d}\eta. \tag{3.2}$$

In figure 3, the given boundary-layer shape factor $H_{12} = \delta_1/\delta_2$ is evaluated in the chordwise system ($H_{12,inc}$ is calculated with the respective incompressible formulations for comparison). The wall-normal density variation in the boundary layer above the roughness and the chordwise variation over the roughness are of the order of 2.7 % and 0.1 %, respectively. For more details on the base flow, see Kurz & Kloker (2014).

3.2. *Stability properties*

Stability properties of the base flow were computed by our in-house linear stability theory (LST) solver, see also Schmidt & Rist (2014). The flow field is decomposed into a steady base flow and an unsteady disturbance field, i.e. $\boldsymbol{q} = (u, v, w, \rho, T)^{\mathrm{T}} = \boldsymbol{q}_b + \boldsymbol{q}'$, with $\boldsymbol{q}$ being a solution to the compressible Navier–Stokes equations, expressed in primitive variables. Parallel flow is assumed and the equations of motion are linearised. Disturbances are considered to be wave-like in the homogeneous ξ and z directions and are represented by Fourier modes

$$\boldsymbol{q}'(\xi, \eta, z, t) = \hat{\boldsymbol{q}}(\eta)\mathrm{e}^{\mathrm{i}(\alpha\xi+\gamma z-\omega t)}, \tag{3.3}$$

with eigenfunction $\hat{\boldsymbol{q}}$, tangential wavenumber $\alpha \in \mathbb{C}$, spanwise wavenumber $\gamma \in \mathbb{R}$, angular frequency $\omega \in \mathbb{R}$ and $\mathrm{i} = \sqrt{-1}$. Since $\alpha = \alpha_r + \mathrm{i}\alpha_i$ is complex, the formulation

https://doi.org/10.1017/jfm.2014.425 Published online by Cambridge University Press

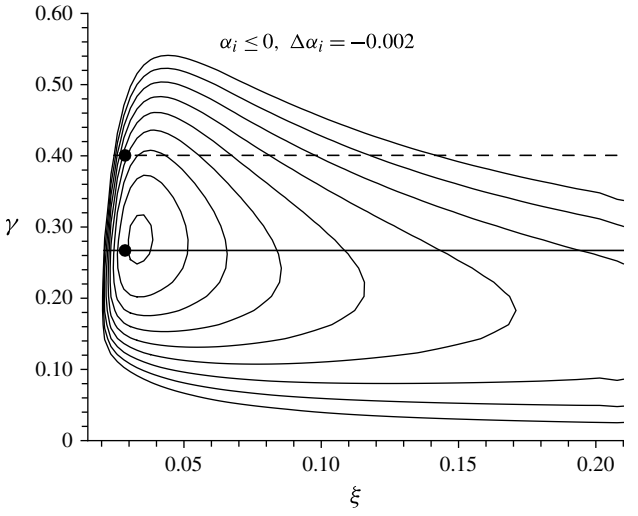


FIGURE 4. Stability diagram for steady CF modes. Here, n-factor integration paths for mode $(0, 1)$, $\gamma_0 = 0.2760$ (solid) and mode $(0, 3/2)$, $\gamma_C = (3/2)\gamma_0 = 0.4006$ (dashed). Black circles: roughness position.

corresponds to a spatial stability problem where disturbances grow with the growth rate $-\alpha_i$ as they travel downstream. The resulting quadratic eigenvalue problem is recast to a first-order problem by the introduction of auxiliary variables – i.e. the eigenvector then reads $\tilde{\boldsymbol{q}} = (\hat{u}, \hat{v}, \hat{w}, \hat{\rho}, \hat{T}, \alpha\hat{u}, \alpha\hat{v}, \alpha\hat{w}, \alpha\hat{T})^{\mathrm{T}}$. The wall-normal direction is resolved with $N = 80$ points using a Chebyshev collocation method, yielding an eigenvalue problem of size $(9N)^2$.

The stability diagram for steady modes based on spatial LST is shown in figure 4. The roughness elements are located slightly downstream of the onset of instability, but upstream of largest amplification. The spanwise domain extent $\lambda_{z,0}$ and the corresponding wavenumber $\gamma_0 = 0.2670$ conform approximately to the wavenumber of the steady mode reaching the highest local amplification rate $|\alpha_i|$. Modes are denoted by the tuple (h, k) with frequency $h\omega_0$ and spanwise wavenumber $k\gamma_0$, with $h, k \in \mathbb{N}_0$, while $h = 0$ for all modes under consideration in this article. As a means to reproduce receptivity amplitudes at the position of the roughness elements, n-factors $n = \int_{\xi}(-\alpha_i)\mathrm{d}\xi$ for modes (0, 1) and (0, 3/2) are integrated along the tangential coordinate ξ.

3.3. *Roughness elements*

The shape of the roughness elements is given by a shallow circular disc, blended smoothly to the undisturbed surface, as can be seen in figure 6(*c*). The roughness contour is defined by a hyperbolic tangent function in polar coordinates

$$\eta_R(r, \phi) = \frac{k}{2}\left(\tanh\left(\frac{S_R}{H_R}\left(\frac{d}{2} - r\right)\right) + 1\right), \quad r \geqslant 0,\ 0 \leqslant \phi < 2\pi, \tag{3.4}$$

with k and d being the nominal height and diameter, respectively, also defining the aspect ratio $r_a = k/d$. The magnitude of the term S_R/H_R controls the maximum slope angle ϕ_R of the element. These elements are referred to as bump elements in the

https://doi.org/10.1017/jfm.2014.425 Published online by Cambridge University Press

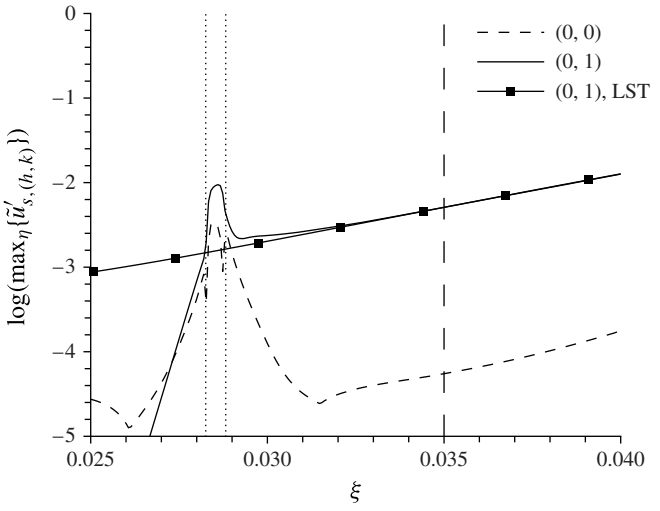


FIGURE 5. Mode evolution for the bump element, $k = 0.05$. Here, $\xi_{ref} = 0.035$: DNS–LST matching.

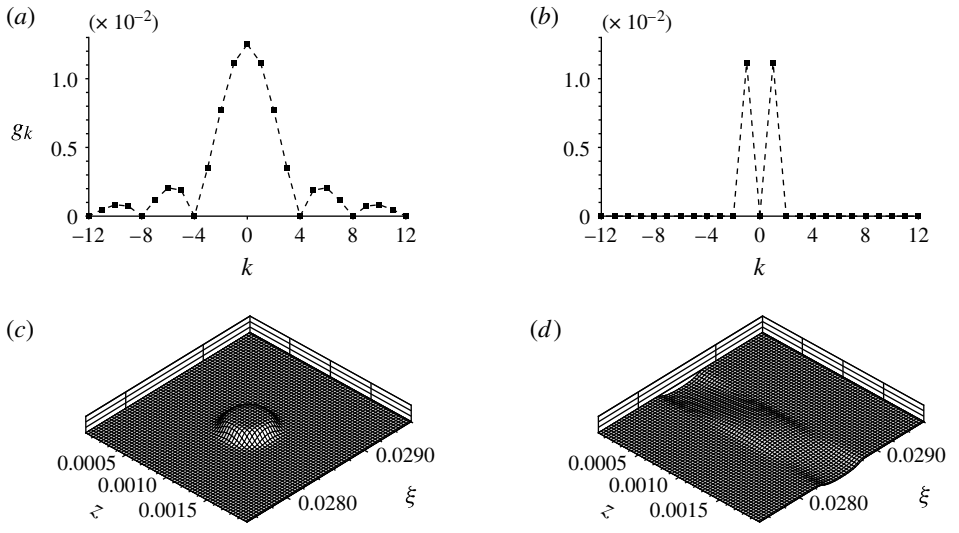


FIGURE 6. Discrete spanwise Fourier spectra g_k corresponding to the centre of the roughness geometry of a bump element (*a*) and a spectrally reduced element $K_R = \{1\}$ (*b*), both with height $k = 0.05$. Meshed bump element (*c*) and spectrally reduced element $K_R = \{1\}$ (*d*), height exaggerated; every second gridline is shown.

following; the respective parameters are given in table 1. For all configurations, the roughness centre is placed at $x_R = 0.0200$, $\xi_R = 0.0285$, $Re_{\delta 1,s} = 500$. The geometry is then transformed to the curvilinear system.

Spanwise Fourier spectra g_k for the roughness centre are shown in figure 7. The spectrum can then be reduced such that only harmonics of interest are kept, as shown in figure 6(*b*), denominated spectrally reduced elements, see also figure 6(*d*). These elements are characterised by the set K_R, containing the retained harmonics

https://doi.org/10.1017/jfm.2014.425 Published online by Cambridge University Press

k	d	r_a	S_R	H_R	ϕ_R (deg.)	χ_p	Re_{kk}
0.01	5.882	0.0017	2.0	1.0	0.57	1.0089	0.01
0.03	5.882	0.0051	2.0	1.0	1.72	1.0269	0.30
0.05	5.882	0.0085	2.0	1.0	2.86	1.0452	0.87
0.07	5.882	0.0119	2.0	1.0	4.00	1.0638	1.65
0.15	5.882	0.0255	2.0	1.0	8.53	1.1414	7.21
0.20	5.882	0.0340	2.0	1.0	11.31	1.1923	12.72
0.30	5.882	0.0510	2.0	1.0	16.70	1.2998	28.07
0.03	3.529	0.0085	2.0	0.6	2.86	1.0452	0.30
0.07	8.235	0.0085	2.0	1.4	2.86	1.0452	1.65

TABLE 1. Shape parameters of investigated roughness elements. For definitions of the parameters, see § 3.3; $Re_{kk} = \bar{k}|\bar{\boldsymbol{V}}(\bar{k})|\bar{\rho}(\bar{k})/\bar{\mu}(\bar{k})$, where $\bar{\boldsymbol{V}}(\bar{k})$ is the velocity vector at $\bar{\eta} = \bar{k}$.

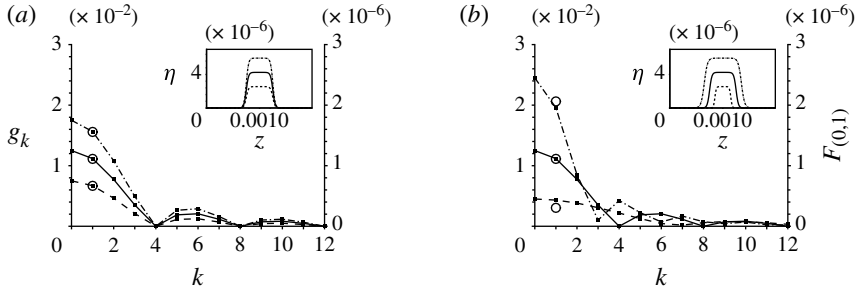


FIGURE 7. Discrete spanwise Fourier spectra g_k corresponding to a cut through the centre of the roughness geometry of a bump element (*a*) and a bump element with constant aspect ratio $r_a = 0.0085$ (*b*), heights $k = 0.03/0.05/0.07$. The large circles show the spectral amplitudes $F_{(0,1)}$ corresponding to the wavevector of mode (0, 1), $\alpha_r = -0.4624$, $\gamma = 0.2670$, obtained from a double Fourier decomposition in ξ and z, cf. (3.8). The insets show crosscuts through the roughness centre.

in multiples of $\pm\gamma_0$. For instance, $K_R = \{0, 1\}$ denotes a roughness element with an associated discrete spanwise spectrum that is non-zero only at 0 and $\pm\gamma_0$.

The maximum slope angle ϕ_R found on the shoulders of the elements is very small, see table 1. Therefore, it is permissible to include the roughness geometry into the volume mesh by elevating the respective surface points along the wall-normal direction to coincide with the roughness geometry under consideration. This causes a local compression of the volume mesh in the wall-normal direction, while originally wall-normal lines remain straight. Indeed, the wall-normal step size remains virtually unchanged, since the compression is relaxed over several boundary layer thicknesses. Grid cells on the shoulders of the elements are distorted; however, the skewness remains small. Extensive, careful grid studies have been performed showing a negligible influence of the grid-point distribution on the results; the standard grid can be regarded as fully sufficient.

The roughness elements were also modelled by a commonly used approach employing inhomogeneous boundary conditions, referred to as the Taylor method hereafter. By means of a Taylor series expansion, truncated after the first-order term, the no-slip and the no-penetration conditions at the rough surface are projected to

https://doi.org/10.1017/jfm.2014.425 Published online by Cambridge University Press

the undisturbed surface and imposed as fixed boundary conditions, see, for example, Tempelmann *et al.* (2012):

$$\boldsymbol{u}(\xi, 0, z) = \boldsymbol{u}_b(\xi, 0, z) - \chi_p \eta_R \left.\frac{\partial \boldsymbol{u}_b}{\partial \eta}\right|_{\eta=0}, \tag{3.5a}$$

$$T(\xi, 0, z) = T_b(\xi, 0, z) - \chi_p \eta_R \left.\frac{\partial T_b}{\partial \eta}\right|_{\eta=0}, \tag{3.5b}$$

where $\boldsymbol{u}$ is the velocity vector, T the temperature, and the subscript b denotes base flow values; χ_p is taken as unity unless otherwise stated. Due to the adiabatic wall boundary condition used for the base flow computation, the wall-normal temperature gradient vanishes, rendering (3.5*b*) trivial. In fact, the wall-normal temperature gradient found in the non-dimensional base flow is five orders of magnitude lower than the velocity gradients. The same holds for the wall-normal pressure distribution and, hence, the density. Accordingly, only velocity components were considered for the definition of the inhomogeneous boundary conditions. This approach was validated by two computations for $k = 0.05$ bump elements, one with only velocity components and one with all primitive variables considered. No deviation in the receptivity amplitude was found.

The inflection point of the present accelerated boundary layer profile lies below the surface, yielding a curvature at the wall. Thus, the linear approximation becomes poor. In order to enhance the modelling quality, a modification of the approach is quantified: for the projection method, we formally augment the Taylor method with higher-order terms. In practice, we extract the velocity components at the desired roughness contour from the undisturbed base flow, negate the values, and prescribe the result at the surface boundary.

Another option for improved accuracy is to multiply the first-order term of the Taylor approach (3.5) by a correction factor, taking into account any shape effects the approach suffers from. Luchini (2013) proposes a protrusion coefficient as function of the shape and the aspect ratio r_a, based on a numerical solution of the Stokes problem, independent of specific boundary-layer characteristics. For smoothed circular cylinders, as used in the present study, an interpolation formula is provided

$$\chi_p = 5.2 r_a + \sqrt{1 + (5.2 r_a)^2}, \tag{3.6}$$

allowing evaluation based on geometrical properties without further knowledge of the underlying wall-bounded flow. Since $r_a = k/d$, χ_p becomes a function of the height k only, if the diameter d remains constant. For $r_a \ll 1$, the quadratic term in the radicand vanishes, leaving the linear function $\chi_p \approx 5.2 r_a + 1$. For the present investigation, we evaluate the full formulation (3.6). This approach is denoted the Taylor method with protrusion coefficient.

3.4. *Receptivity coefficient*

Receptivity coefficients are commonly defined as the ratio of the effective disturbance response to an appropriate measure for the input amplitude. This definition corresponds to the linearised receptivity theory for the exitation of crossflow instabilities by localised surface roughness, as outlined by Choudhari & Streett (1990). For the receptivity coefficient, we transform the velocity components to an edge-streamline-oriented coordinate system, normalise the results by the magnitude of the local

https://doi.org/10.1017/jfm.2014.425 Published online by Cambridge University Press

base-flow edge-velocity (tilde denotes normalised values), and take the wall-normal disturbance maximum of mode (0, 1). The initial disturbance amplitude precisely at the roughness ($\xi_R = 0.0285$) cannot be determined directly, but can be reconstructed by matching an n-factor curve for the respective mode to the DNS result at $\xi_{ref} = 0.0350$, where near-wake effects have decayed, see figure 5. This procedure implies an exponential growth behaviour and is valid for amplitudes at ξ_{ref} not much larger than approximately 0.01. Taking into account the increasing edge velocity of the accelerated boundary layer, the receptivity amplitude is then given by

$$A_{(0,1)} = \max_{\eta} \left\{ \tilde{u}'_{s,(0,1),ref} \right\} \exp\left(n_R - n_{ref}\right) \frac{u_{b,s,e,ref}}{u_{b,s,e,R}} = \max_{\eta} \left\{ \tilde{u}'_{s,(0,1),ref} \right\} B. \tag{3.7}$$

Again, the subscript s refers to velocity components in the edge-streamline-oriented coordinate system, e denotes quantities at the boundary-layer edge, R and ref indicate values at the roughness and the reference position, respectively, and (0, 1) refers to the excited steady crossflow vortex; n-factor curves are obtained from the LST computations, cf. § 3.2. Following (3.7), the upstream extrapolation reduces to a multiplication by the constant factor B, independent of the measured amplitude.

The disturbance input is characterised by the modal amplitude of the roughness geometry associated with the wavevector of mode (0, 1), $\alpha_r = -0.4624$, $\gamma = 0.2670$ at the roughness position. The spectrum of the roughness geometry is obtained from a Fourier series expansion in z and a subsequent Fourier transform in ξ such that the roughness contour is expressed by an integral and a sum over the complex coefficients $\hat{f}(\alpha_r, k\gamma_0) = f(\alpha_r, k\gamma_0)\mathrm{e}^{\mathrm{i}\Theta(\alpha_r, k\gamma_0)}, f \in \mathbb{R}$:

$$\eta_R(\xi, z) = \int_{-\infty}^{\infty} \sum_{k=-K}^{K} \hat{f}(\alpha_r, k\gamma_0)\mathrm{e}^{\mathrm{i}(\alpha_r \xi - k\gamma_0 z)} \mathrm{d}\alpha_r, \tag{3.8}$$

with the continuous tangential wavenumber $\alpha_r \in \mathbb{R}$, the discrete spanwise wavenumber $k\gamma_0$, the number of spanwise modes K, and $\mathrm{i} = \sqrt{-1}$. The associated physical amplitude is given by

$$F(\alpha_r, k\gamma_0) = 2f(\alpha_r, k\gamma_0), \quad \text{for } \alpha_r \neq 0 \text{ or } k \neq 0. \tag{3.9}$$

For clarity, we define $F_{(0,1)} = F(\alpha_{r,(0,1)}, \gamma_0)$; results for selected roughness elements are depicted by circles in figure 7. For the bump elements in figure 7(*a*), $F_{(0,1)}$ is proportional to g_1 and equivalently to k. However, for bump elements with constant aspect ratio (cf. figure 7*b*), g_1 increases superlinearly with k, and $F_{(0,1)}$ is no longer proportional to g_1 because the α_r-spectrum also changes. Now, the spectral receptivity coefficient for a given roughness element can be defined as

$$C_{R,(0,1)} = \frac{A_{(0,1)}}{F_{(0,1)}}. \tag{3.10}$$

In order to validate our results for other spanwise wavenumbers, we chose the control mode (0, 3/2), $\alpha_r = -0.6993$, $\gamma = 0.4006$, with $\gamma_C = (3/2)\gamma_0$ as the second test case. This mode is of particular interest for the stabilisation of swept-wing boundary layers by distributed discrete roughness elements, as proposed by Saric *et al.* (1998). The associated receptivity coefficient is defined as previously; however, the receptivity amplitude $A_{(0,3/2)}$ is evaluated with respect to $\tilde{u}'_{s,(0,3/2),ref}$ and the corresponding n-factor curve; Fourier coefficients respresenting the spectrum of

https://doi.org/10.1017/jfm.2014.425 Published online by Cambridge University Press

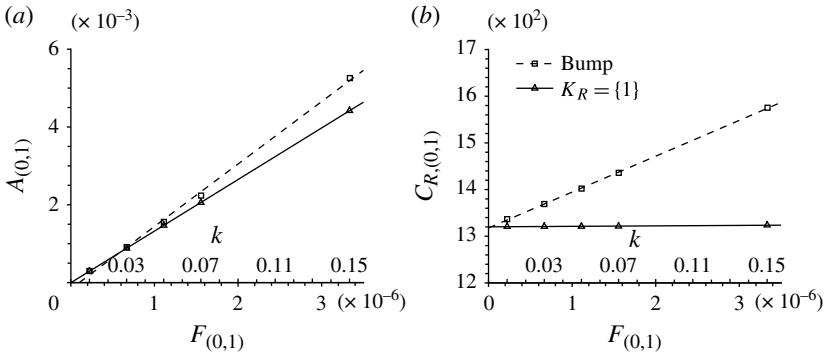


FIGURE 8. Receptivity amplitudes (*a*) and receptivity coefficients (*b*) for mode (0, 1), for bump elements and spectrally reduced elements of type $K_R = \{1\}$, heights $k = 0.01/0.03/0.05/0.07/0.15$. Symbols: DNS results. Lines: linear curve fits.

the roughness shape are now associated with multiples of γ_C, i.e. $\hat{f}(\alpha_r, k\gamma_C)$, and $F_{(0,3/2)} = F(\alpha_{r,(0,3/2)}, \gamma_C)$. Altogether, the receptivity coefficient for mode (0, 3/2) reads

$$C_{R,(0,3/2)} = \frac{A_{(0,3/2)}}{F_{(0,3/2)}}. \tag{3.11}$$

For small roughness elements, receptivity is often said to be linear, implying a constant receptivity coefficient.

4. Results

4.1. *Meshed roughness elements*

DNS on the fine grid with $k = 0.01/0.03/0.05/0.07/0.15$, cf. figure 7(*a*), were performed for both the bump elements and the spectrally reduced elements with $K_R = \{1\}$; receptivity amplitudes according to (3.7) are given in figure 8(*a*) (symbols). Up to $k = 0.03$, the results for the bump elements and the $K_R = \{1\}$ elements seem to coincide, while for larger heights the bump shape yields an increasing deviation to higher values. A linear curve fit of the bump results fails, while the data from the $K_R = \{1\}$ case are well approximated by a line through the origin. The question whether a linear range exists for small bump elements can be examined by the behaviour of the receptivity coefficient for different element heights, see figure 8(*b*). For $K_R = \{1\}$, the coefficient remains constant without any evidence of a changing behaviour for higher elements. The receptivity coefficient for the bump element coincides with this value in the limit of vanishing roughness height; however, it appears to be a linear function of the latter. This behaviour indicates a significant quadratic content in the flow response, even for bump elements with a height below 1 % of the local displacement thickness. For $k = 0.10$, suggested as the limit for linear receptivity by Tempelmann *et al.* (2012), the deviation from the constant value found for $K_R = \{1\}$ reaches 12 %, although the spectral input from the roughness geometry is identical in both cases. The difference can be attributed at first sight to the presence of the 2D part (0, 0) and higher harmonics $(0, k)$, $k > 1$, in the geometry of the bump element. Thus, the flow responds in a nonlinear manner, as predicted by Choudhari & Duck (1996) using asymptotic theory.

Two possible explanations for the nonlinearity in the receptivity amplitudes come to mind: (i) the local stability properties of the base flow behind the element are altered

https://doi.org/10.1017/jfm.2014.425 Published online by Cambridge University Press

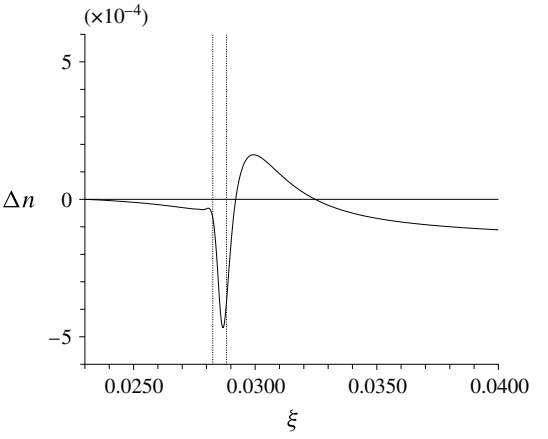


FIGURE 9. n-factor alteration for mode (0, 1) due to the introduction of a spectrally reduced element with $K_R = \{0\}$.

by mode (0, 0), cf. figure 5, such that the mode under consideration (0, 1) experiences higher amplification rates compared to the undisturbed base flow. Our reconstruction of the receptivity amplitude precisely at the position of the roughness does not capture such near-wake effects and therefore overpredicts the actual value. (ii) The receptivity to mode (0, 1) itself is altered owing to the presence of (0, 0) and higher modes.

The former effect has been assessed by means of both linear stability analysis and DNS. A spectrally reduced element with $k = 0.05$ and $K_R = \{0\}$, which is a pure 2D roughness, has been introduced at the usual position. The stability properties of the resulting 2D flow were analysed by LST and compared to the results for the unperturbed flow. Figure 9 shows the deviation of the n-factors obtained from the flow with the $K_R = \{0\}$ element and the base flow, respectively – i.e. positive values indicate increased amplitudes due to the roughness. In fact, the spectrally reduced element with $K_R = \{0\}$ leads to a slightly negative value of $\Delta n = -6.9132 \times 10^{-5}$ at the reference position $\xi_{ref} = 0.0350$.

A second analysis by means of DNS features a (0, 1) disturbance, triggered by a zero-mass-flux disturbance strip at the wall at $\xi = 0.0242$, upstream of the usual roughness position. We prescribe the vertical mass flux ρv_g, modulated in the periodic z direction, with a smooth envelope in the downstream direction. The amplitude is sufficiently small to ensure linear growth of the resulting disturbance. Two DNS have been performed: a reference case with a smooth wall, and a second case with a $k = 0.05/K_R = \{0\}$ element at the usual roughness position in order to generate a base flow deformation (0, 0), cf. figure 10 (dashed lines). In the latter case, the close vicinity of the roughness element shows a direct influence of the roughness on mode (0, 0), while the downstream growth is generated nonlinearly by (0, 1). However, mode (0, 1) proves to be virtually unaffected by the presence of the roughness element, and leads to the same disturbance evolution as in the smooth-wall case, as can be seen from the solid lines in figure 10. The deviation from the reference case at $\xi_{ref} = 0.035$ is as small as 0.016 %. Hence, the mode (0, 0) with an amplitude of 0.005 does not alter the stability characteristics, as has also been found for suction, where a mode (0, 0) amplitude of up to approximately 0.010 has virtually no effect on the stability either, see, for example, Messing & Kloker (2010).

https://doi.org/10.1017/jfm.2014.425 Published online by Cambridge University Press

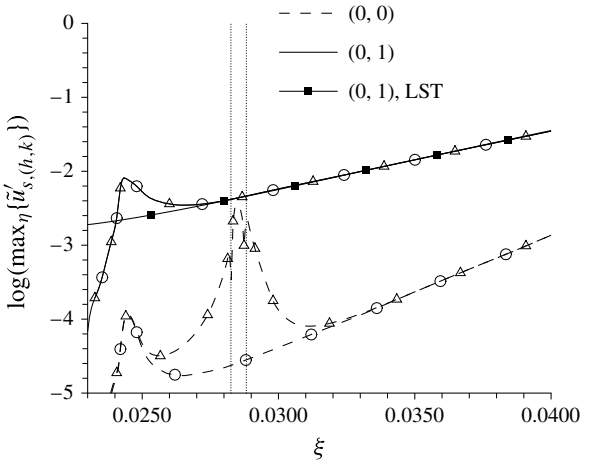


FIGURE 10. Evolution of the test mode (0, 1). Smooth wall set-up (circles), set-up with $K_R = \{0\}$ (triangles).

The theoretical approach by Choudhari & Duck (1996) shows a decoupling of the wall-normal regions of inviscid crossflow instability and receptivity. Therefore, nonlinear receptivity may set in before a significant modification of the stability characteristics is observed. Accordingly, our DNS confirms the asymptotic scaling approach.

To complete the picture, the spectral content of the spectrally reduced element is altered. Results for the receptivity coefficients are given in figure 11, where the previous results from figure 8(*b*) are included again. First, we add the 2D part to get $K_R = \{0, 1\}$. The resulting data are again approximated well by a linear curve fit. Although the slope is not as steep as for the bump shape, the tendency is the same – i.e. the receptivity coefficient is a linear function of the roughness height. The effect becomes even stronger as we further add the second spanwise harmonic to the roughness shape, i.e. $K_R = \{0, 1, 2\}$. Now, the results perfectly resemble the findings from the bump elements. We note that elements with the modal content $K_R = \{0, 1, 2\}$ reach the same physical element height as the bump elements. This is a special feature of the shape of the bump elements under consideration, and will not be the case for other ratios of diameter to spanwise spacing, $d/\lambda_{z,0}$.

Results for the second spanwise wavenumber under consideration, $\gamma_C = (3/2)\gamma_0$, are provided in figure 12. Here, $K_R = \{3/2\}$ contains only the fundamental spanwise harmonic, while $K_R = \{0, 3/2, 3\}$ also comprises the 2D part and the first higher harmonic (equivalent to $K_R = \{1\}$ and $K_R = \{0, 1, 2\}$ in the γ_0 case, respectively). The overall level of receptivity is enhanced, nevertheless the qualitative behaviour perfectly resembles the data obtained for γ_0: the bump element yields a rising receptivity coefficient for increasing roughness height, with the same slope as found for γ_0; receptivity to the $K_R = \{3/2\}$ elements is perfectly linear. The result for $K_R = \{0, 3/2, 3\}$ does not coincide with the bump for this spanwise spacing; however, the tendency is the same as in the case of mode (0, 1). Note that the spanwise spectrum of the roughness for γ_C differs qualitatively from the spectrum for γ_0, in particular the proportions between the harmonics are different. Altogether, the consistency of the general superlinear behaviour for a different spectral shape is proved.

https://doi.org/10.1017/jfm.2014.425 Published online by Cambridge University Press

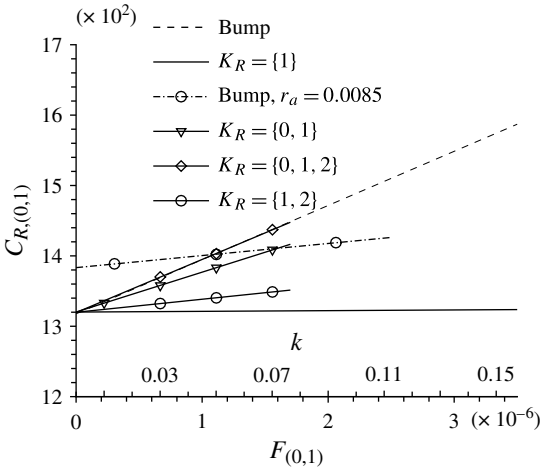


FIGURE 11. Receptivity coefficients for mode (0, 1), k-axis not valid for a bump with fixed aspect ratio $r_a = 0.0085$. Symbols: DNS results. Lines: linear curve fits.

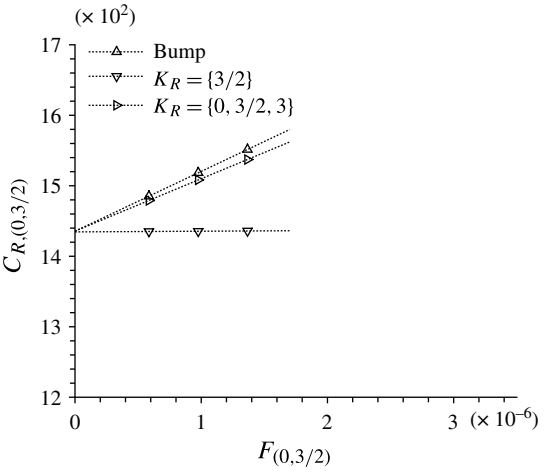


FIGURE 12. Receptivity coefficients for mode (0, 3/2). Symbols: DNS results. Lines: linear curve fits.

Coming back to the γ_0 set-up and figure 11, the introduction of spectrally reduced elements with $K_R = \{1, 2\}$ to the flow illustrates again that the present findings cannot be traced back to altered stability properties due to a 2D base flow deformation and also not to the 2D part as such. Although the elements do not comprise a 2D part, the receptivity coefficient still deviates from the constant value found for $K_R = \{1\}$. Rather, the investigated combinations suggest that every additional spanwise harmonic contributes to the slope of the receptivity coefficient, especially if they alter the maximum height of the (reduced) element. In the present case, it even appears that these contributions can be superposed in a linear manner – i.e. the slopes obtained from $K_R = \{0, 1\}$ and $K_R = \{1, 2\}$ yield the slope of $K_R = \{0, 1, 2\}$.

https://doi.org/10.1017/jfm.2014.425 Published online by Cambridge University Press

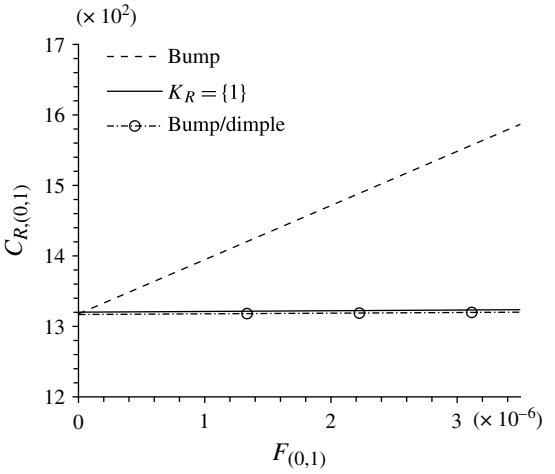


FIGURE 13. Receptivity coefficients for mode (0, 1), alternating bump/dimple elements. Symbols: DNS results. Lines: linear curve fits.

When looking at the physical shapes of the investigated roughness elements, it is apparent that the $K_R = \{1\}$ elements reveal a symmetry with respect to the smooth-wall surface in the sense that the positive and the negative deformation have the same shape. Presuming the positive part constitutes an obstacle that blocks some flow, the negative part would compensate for the blockage by letting pass more flow. In this simple model, both the positive and the negative blockage would scale nonlinearly with the height of the local deformation, due to the wall-normal velocity gradient. Were a zero spanwise mean of the blockage the requirement for linear receptivity (as is the case for $K_R = \{1\}$), the most straightforward way to obey this rule would be the construction of a symmetric roughness in the previous sense. One obvious test case for this supposition is to augment the original periodic bump array with additional bumps with negated height, i.e. dimples, in between. Thereby, the spanwise mean becomes zero, and the corresponding spanwise spectrum is non-zero only for $k = \pm(2n - 1)$, $n \in \mathbb{N}^+$. Results for such a configuration with alternating bumps and dimples are shown in figure 13. Not only does the receptivity coefficient stay constant for the three investigated heights $k = 0.03/0.05/0.07$, but also the absolute values are in accordance with the results for $K_R = \{1\}$.

Theoretical results published in Smith *et al.* (1981), Smith (1991), Choudhari & Duck (1996), Lipatov & Vinogradov (2000) and recent findings by Luchini (2013) indicate a nonlinear connection between the roughness height and the disturbance velocity at the wall, used to model the roughness by means of inhomogeneous boundary conditions. The protrusion coefficient defined in the latter work for various roughness shapes is a function of the corresponding aspect ratio r_a, and therefore also a function of the height if the diameter is kept constant. Although the protrusion coefficient is, in the first place, supposed to account for a poorer modelling quality at higher aspect ratios and does not directly relate to the receptivity coefficient, its dependence on the element height shows a remarkable similarity to our findings. To shed some light on a possible connection and see if the superlinear behaviour is an effect of the aspect ratio, the bump element with $k = 0.05$, $r_a = 0.0085$, was taken as reference, and two bump elements with $k = 0.03$ and $k = 0.07$, respectively,

https://doi.org/10.1017/jfm.2014.425 Published online by Cambridge University Press

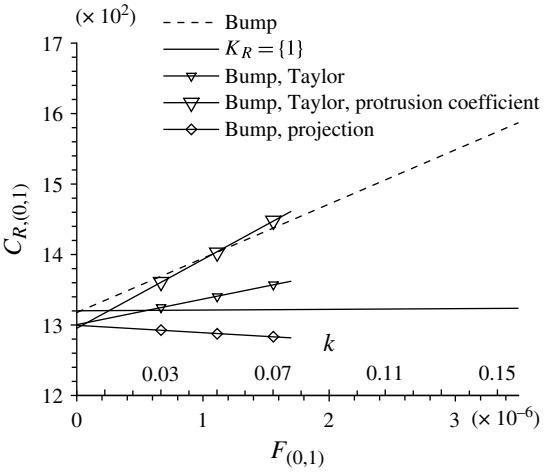


FIGURE 14. Same as figure 11, but with modelled roughness.

and the same r_a were introduced into the boundary layer. Self-similarity of this set of elements is ensured by a proper scaling of H_R, cf. table 1 and figure 7(*b*) (inset). Figure 11 reveals a clearly weaker dependence of the receptivity coefficient on the spectral element height $F_{(0,1)}$, although the slope is non-zero. We note that the evaluation of the protrusion coefficient by Luchini (2013) does not include 3D boundary-layer characteristics.

4.2. *Modelled roughness elements*

We now compare the three modelling approaches outlined in § 3.3. Simulations with modelled roughness elements are performed on the standard grid. We consider bump elements and spectrally reduced elements with $K_R = \{1\}$ and $K_R = \{1, 2\}$; the investigated heights are $k = 0.03/0.05/0.07$. Although the absolute values differ, the receptivity coefficients obtained from the Taylor approach show a similar behaviour as found for the meshed roughness elements, see figures 14 and 15: for the bump element, the receptivity coefficient increases with growing element height, while for the $K_R = \{1\}$ element (cf. figure 15) it remains constant. When applying the Taylor method with protrusion coefficent, the values are close to the results from the meshed roughness for the shown element heights. The projection method, despite being considered a more accurate modelling approach, is not capable of reproducing the increasing receptivity coefficient. Whenever the roughness lacks a 2D part, both the Taylor and the projection method yield constant receptivity coefficients; a summary of such results is given in figure 15.

In summary, the receptivity coefficient of all modelled roughness elements reveals only a weak dependence on the modal roughness height. This is in accordance with results provided by Tempelmann *et al.* (2012), obtained when using a modelling technique similar to our Taylor approach. They find linearly increasing receptivity amplitudes for circular roughness elements, for heights up to $k = 0.60$.

4.3. *Range of validity*

The applicability of inhomogeneous boundary conditions as a means to model discrete roughness elements is limited to small roughness elements; however, the

https://doi.org/10.1017/jfm.2014.425 Published online by Cambridge University Press

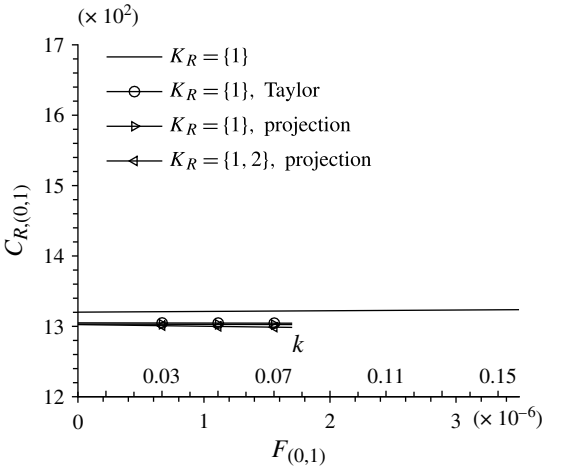


FIGURE 15. Receptivity coefficients for mode (0, 1), modelled spectrally reduced elements. Symbols: DNS results. Lines: linear curve fits.

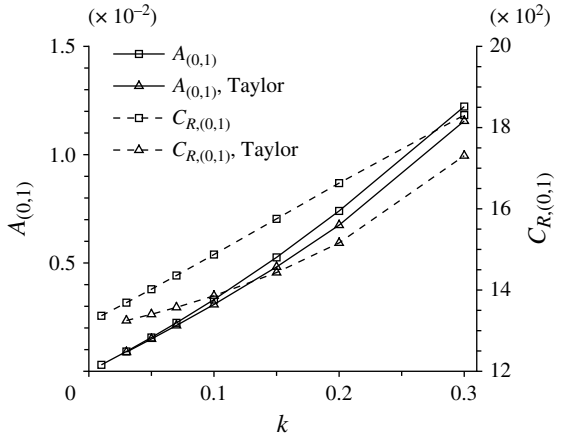


FIGURE 16. Receptivity amplitudes and coefficients for mode (0, 1), meshed and modelled bumps. Symbols: DNS results.

upper boundary has still to be determined. The receptivity behaviour for larger bump elements up to $k = 0.30$ is depicted in figure 16 for the meshed case and the Taylor case. For larger elements, our method to reproduce the receptivity amplitudes at the roughness elements is no longer valid due to nonlinear saturation of mode (0, 1); furthermore, the flow in close proximity to the element starts to differ qualitatively between meshed and modelled roughness. In the considered range, the receptivity amplitudes $A_{(0,1)}$ obtained from meshed and modelled roughness show the same superlinear behaviour. With the modelled roughness, the measured amplitude at $k = 0.10$ is 6.5 % below the value for the meshed roughness, and at $k = 0.15$ the deviation is already 8.4 %.

https://doi.org/10.1017/jfm.2014.425 Published online by Cambridge University Press

5. Conclusions

A detailed DNS study on the receptivity of a three-dimensional boundary layer on a swept wing to a spanwise array of shallow circular roughness elements has been performed. The motivation was recent experimental and numerical results concluded to show a linear increase in the amplitudes of steady crossflow modes with the height of those elements at constant diameter. However, it turns out that the amplitude of the most amplified steady crossflow mode at a reference station downstream clearly scales superlinearly with the element height at constant diameter, as predicted by theoretical results based on large-Reynolds-number asymptotic theory. The position of the reference station excludes ongoing transient growth effects. Thus the receptivity coefficient is not a constant, but rather a linear function of the roughness modal amplitude in this situation; this holds for element heights up to at least 30 % of the local displacement thickness at the considered Reynolds number $Re_{\delta 1,s} = 500$. Only for roughness shapes that consist of alternating bumps and dimples of equal shape and size, and thus have zero spanwise mean, is a constant receptivity coefficient found. However, a zero spanwise mean of the shape is not sufficient: if the spanwise bump/dimple structure has differing heights and depths, but still zero spanwise mean, the receptivity is again nonlinear. Evidently, the 'flow blockage' is decisive, scaling nonlinearly with the roughness height (or depth) due to the wall-normal gradient of the streamwise velocity: whenever the spanwise mean of the blockage is non-zero, the receptivity is nonlinear. For increasing element height at constant aspect ratio, the superlinearity is virtually negligible; recent theoretical results by Luchini (2013), suggesting that the superlinearity is closely connected to the changing aspect ratio with increasing element height, are therefore confirmed. For high elements it is known that the roughness Reynolds number Re_{kk}, based on the variables taken at the roughness height in the undisturbed boundary layer, is a meaningful parameter, and this scales approximately quadratically with the roughness height k. This quadratic influence basically exists already at small heights, but is not yet dominant in this 'linear' regime.

Acknowledgements

This work has been supported by the European Commission through the FP7 project 'RECEPT' (grant agreement no. ACPO-GA-2010-265094). The provision of computational resources by the Federal High-Performance Computing Center Stuttgart (HLRS) is gratefully acknowledged.

REFERENCES

BABUCKE, A. 2009 Direct numerical simulation of noise-generation mechanisms in the mixing layer of a jet. PhD thesis, University of Stuttgart.

BERTOLOTTI, F. P. 2000 Receptivity of three-dimensional boundary-layers to localised wall roughness and suction. *Phys. Fluids* **12** (7), 1799–1809.

BODONYI, R. J., WELCH, W. J. C., DUCK, P. W. & TADJFAR, M. 1989 A numerical study of the interaction between unsteady free-stream disturbances and localised variations in surface geometry. *J. Fluid Mech.* **209**, 285–308.

BOGOLEPOV, V. V. 1986 A general scheme for three-dimensional local flow regimes. *PMTF Zh. Prikl. Mekh. Tekh. Fiz.* **6**, 80–91.

BORODULIN, V. I., IVANOV, A. V., KACHANOV, Y. S. & ROSCHEKTAEV, A. P. 2013 Receptivity coefficients at excitation of cross-flow waves by free-stream vortices in the presence of surface roughness. *J. Fluid Mech.* **716**, 487–527.

https://doi.org/10.1017/jfm.2014.425 Published online by Cambridge University Press

CHOUDHARI, M. & DUCK, P. W. 1996 Nonlinear excitation of inviscid stationary vortex instabilities in a boundary-layer flow. In *IUTAM Symposium on Nonlinear Instability and Transition in Three-Dimensional Boundary Layers*, pp. 409–422.

CHOUDHARI, M. & STREETT, C. L. 1990 Boundary layer receptivity phenomena in three-dimensional and high-speed boundary layers. *AIAA Paper* 90-5258.

COLONIUS, T., LELE, S. K. & MOIN, P. 1993 Boundary conditions for direct computation of aerodynamic sound generation. *AIAA J.* **31** (9), 1574–1582.

FRIEDERICH, T. A. & KLOKER, M. J. 2011 Control of crossflow-vortex induced transition: DNS of pinpoint suction. AIAA Paper 2011-3884.

FRIEDERICH, T. A. & KLOKER, M. J. 2012 Control of the secondary cross-flow instability using localised suction. *J. Fluid Mech.* **706**, 470–495.

GAITONDE, D. V. & VISBAL, M. R. 1998 High-order schemes for Navier–Stokes equations: algorithm and implementation into FDL3DI. *Tech Rep. DTIC Document*.

GAPONENKO, V. R., IVANOV, A. V., KACHANOV, Y. S. & CROUCH, J. D. 2002 Swept-wing boundary-layer receptivity to surface non-uniformities. *J. Fluid Mech.* **461**, 93–126.

GILES, M. B. 1990 Non-reflecting boundary conditions for Euler equation calculations. *AIAA J.* **28** (12), 2050–2058.

HILL, D. C. 1995 Adjoint systems and their role in the receptivity problem for boundary layers. *J. Fluid Mech.* **292**, 183–204.

HUNT, LAUREN. E. & SARIC, WILLIAM. S. 2011 Boundary-layer receptivity of three-dimensional roughness arrays on a swept-wing. *AIAA Paper* 2011-3881.

KELLER, M. A. & KLOKER, M. J. 2013 DNS of effusion cooling in a supersonic boundary-layer flow: influence of turbulence. *AIAA Paper* 2013-2897.

KURIAN, T., FRANSSON, J. H. M. & ALFREDSSON, P. H. 2011 Boundary layer receptivity to free-stream turbulence and surface roughness over a swept flat plate. *Phys. Fluids* **23** (3), 034107.

KURZ, H. B. E. & KLOKER, M. J. 2014 Effects of a discrete medium-sized roughness in a laminar swept-wing boundary layer. In *New Results in Numerical and Experimental Fluid Dynamics IX* (ed. A. Dillmann), Notes on Numerical Fluid Mechanics and Multidisciplinary Design, vol. 124, pp. 1–8. Springer.

LIPATOV, I. I. & VINOGRADOV, I. V. 2000 Three-dimensional flow near surface distortions for the compensation regime. *Phil. Trans. R. Soc. Lond.* **358** (1777), 3143–3153.

LUCHINI, P. 2013 Linearised no-slip boundary conditions at a rough surface. *J. Fluid Mech.* **737**, 349–367.

MESSING, R. & KLOKER, M. J. 2010 Investigation of suction for laminar flow control of three-dimensional boundary layers. *J. Fluid Mech.* **658**, 117–147.

SARIC, W. S., CARRILLO, R. B. JR & REIBERT, M. S. 1998 Leading-edge roughness as a transition control mechanism. *AIAA Paper* 98-0781.

SCHMIDT, O. T. & RIST, U. 2014 Viscid-inviscid pseudo-resonance in streamwise corner flow. *J. Fluid Mech.* **743**, 327–357.

SCHWAMBORN, D., GERHOLD, T. & HEINRICH, R. 2006 The DLR TAU-code: recent applications in research and industry. In *European Conference on Computational Fluid Dynamics, ECCOMAS CFD, TU Delft, The Netherlands* (ed. P. Wesseling, E. Oñate & J. Périaux).

SMITH, F. T. 1991 Steady and unsteady 3-D interactive boundary layers. *Comput. Fluids* **20** (3), 243–268.

SMITH, F. T., BRIGHTON, P. W. M., JACKSON, P. S. & HUNT, J. C. R. 1981 On boundary-layer flow past two-dimensional obstacles. *J. Fluid Mech.* **113**, 123–152.

TEMPELMANN, D., SCHRADER, L.-U., HANIFI, A., BRANDT, L. & HENNINGSON, D. S. 2012 Swept wing boundary-layer receptivity to localised surface roughness. *J. Fluid Mech.* **711**, 516–544.

WASSERMANN, P. & KLOKER, M. 2002 Mechanisms and passive control of crossflow-vortex-induced transition in a three-dimensional boundary layer. *J. Fluid Mech.* **456**, 49–84.

https://doi.org/10.1017/jfm.2014.425 Published online by Cambridge University Press